Identification of the coefficient of sliding friction from an apparent non-Coulomb behavior between wood and steel
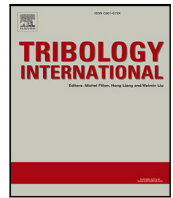
Zheng, Yi; Cabboi, Alessandro; Kuilen, Jan Willem van de

Important note
To cite this publication, please use the final published version (if applicable).
Please check the document version above.

Contents lists available at ScienceDirect

Tribology International

journal homepage: www.elsevier.com/locate/triboint

Full Length Article

Identification of the coefficient of sliding friction from an apparent non-Coulomb behavior between wood and steel

Yi Zheng [a,*], Alessandro Cabboi [a], Jan-Willem van de Kuilen [a,b]

[a] *Department of Engineering Structures, Faculty of Civil Engineering and Geosciences, Delft University of Technology, Stevinweg 1, Delft, 2628CN, Netherlands*
[b] *Wood Research Munich, Technical University of Munich, Munich, 80797, Germany*

ARTICLE INFO

ABSTRACT

This study investigates the sliding friction fluctuations through hysteresis cycles, observed between a steel sphere and wood specimens of beech and spruce, by using a tribometer and a profilometer. At first, the tracked wear profiles revealed a correlation between the normal force variation and the surface waviness. However, the normal force variation alone was not able to explain the observed friction force fluctuation. Hence, to explain most of the observed non-Coulomb friction hysteresis behavior, the wear-scar interaction is taken into account through an optimization framework used for data post-processing and leading to an optimal friction coefficient. A comparative study showed similar values between the identified optimal friction coefficient, the mean and energy-based friction coefficients.

1. Introduction

In recent years, the lightweight and renewable properties of wood raised a new interest in using wood to replace conventional construction materials, whose recycling costs and overall environmental impact can be rather high [1,2]. In the perspective of replacing traditional construction materials, one of the current challenges in the wood construction industry concerns the design of high-rise buildings, which are mostly built with concrete and steel. At the moment, the height of wood high-rise buildings has successfully reached 85 m [3,4], while taller solutions up to 150 m are also in an advanced design stage [3,5]. Besides civil engineering applications, the "greener" character of wood, combined to its unique mechanical properties, also offer solutions to use wood as bearings or friction dampers [6–10]. A common trait for all the aforementioned applications, concerns their susceptibility towards dynamic loads, either characterized by small or large displacements. Such cyclic loads may show the most pronounced effects at joints and interfaces. While on the one hand, joints and interfaces are prone to fretting fatigue, degradation and relaxation processes, on the other hand, if properly designed, they can significantly contribute to enhance ductility and to increase the capability of dissipating energy. It goes without saying that, to properly design joints and interfaces, it becomes essential to characterize beforehand their frictional and wear behavior, which can govern part of the mechanical response [11–17].

To carry out a tribological characterization focused on measuring the frictional resistance, tests such as linear sliding friction, reciprocating sliding friction or rolling friction are commonly adopted for wood.

Examples of such linear sliding friction, for which the sliding speed remains constant, and rolling friction, were reported by Atack and Tabor [18], who investigated the tribological pairing between balsam fir wood and steel, and balsam fir wood and polytetrafluoroethylene (PTFE), both pairs in dry and wet conditions. Due to the viscoelastic nature of wood, they found that the sliding friction force of wood can be expressed by the sum of the hysteretic term and the interfacial adhesion resistance term. One of the main outcomes was the strong dependency between the coefficient of friction (COF) for a PTFE sphere sliding on balsam fir wood, and the moisture content of the wood specimens. Whereas only a marginal difference was observed for the friction coefficient of a steel sphere sliding on balsam fir wood for different moisture conditions. McLaren and Tabor [19] studied the sliding friction between a steel ball and wood specimens of lignum vitae, and the results indicated that the coefficient of friction of such pairing is comparably small as a steel ball - PTFE interaction (a material pair known for its low COF, usually $\mu < 0.1$), due to a thin film of wood-wax naturally extruded during the sliding process. To go beyond the influence of moisture and intrinsic lubricants, McKenzie and Karpovich [20] tested the influence of the sliding speed, the normal load, the nominal contact area, the roughness of steel and the fiber direction on the frictional properties between a large variety of wood species and steel. The results show that each of these factors can lead to changes, while the more significant factors are the sliding speed and moisture content of the wood specimen. Lemoine et al. [21]

studied the sliding friction behavior between spruce pine and steel, for different moisture content, density, presence of extractives in wood and for different sliding directions with reference to the radial and transverse plane. Most of the averaged COF values reported in [21], range between 0.16–0.26 for which the minimum was observed for sliding parallel to the growth rings (and unextracted wood), and the maximum was measured for sliding perpendicular to the growth rings (for extractive-free wood). A wider range of the COF, between 0.1–0.9, was reported in [22], where friction tests between steel and pine, spruce, and sapwood were carried out, for different varying factors such as moisture content, surface roughness, sliding speed and duration of sliding. A similar wide range of the COF was also observed by Vaz and Fortes [23], who tested the frictional behavior of cork specimens sliding on steel and glass. The influence of temperature on the frictional resistance between a rotating steel disc in contact with spruce specimens was shown in [24,25], in which tests were carried out in a pressurized saturated steam environment. The COF of the material pair was found to be significantly influenced by the temperature and the moisture content, showing values ranging between 0.4 and 0.9. A COF range between 0.34 and 1.01 was also observed in [6], for sliding frictional pairs formed by a steel ring and lignum vitae, black fiber palm and spruce plates, tested at different sliding directions. It is worth noting that the steel lignum vitea pair showed the highest COF, around 1, regardless of the sliding direction, while the spruce specimen showed the largest variation between sliding directions. In all the aforementioned studies, despite the large differences of the COF and variety of test results, almost all authors agree on the contribution of the adhesion (implying the dependency on the real contact area) and hysteresis terms to the friction force, when it comes to interpret friction results for wood specimens.

Contrary to linear sliding friction tests, the sliding speed of reciprocating friction tests oscillates between zero and a maximum, involving velocity reversals and periodic stick to slip transitions. Such type of tests are usually carried out for characterizing the fretting wear behavior of the material pairs, in combination with measured frictional forces. Reciprocating sliding tests were shown in [7,8], in which the wear behavior and the variation of the COF for different sliding directions, with reference to the fiber orientations, were investigated.

A common missing element in most of the studies on wood-related friction found in the literature, consists of a clear and systematic procedure on how to post-process the results from friction tests, considering the complexity of the wood's anatomy. For example, in the mechanical engineering community, reciprocating friction tests are also commonly used, and friction hysteresis curves showcasing the relation between the measured friction force and the sliding displacement per cycle, provide a good starting point to understand the frictional properties, wear behavior and corresponding dissipated energy of the tested material pairs. For a detailed discussion on how to interpret hysteresis curves, see [26–28]. Therefore, this study aims to bridge the gap between how results are usually interpreted between the different research communities, discussing the use of reciprocating sliding and corresponding hysteresis curves to characterize the frictional behavior of wood-related material pairs. Specifically, this study focuses on the material pair formed by a steel sphere and wood samples constituted by European beech (Fagus sylvatica) and spruce (Picea abies). Tests are carried out at a constant reciprocating sliding frequency, fixed normal load and stroke length, and for different wood planes and sliding directions. Surface measurements of wear grooves on the wood surfaces were also performed. The measured results show hysteresis curves characterized by an "apparent" non-Coulomb sliding friction behavior, which may suggest strong variations of the coefficient of friction, since the fluctuations in the measured normal forces are not large enough to explain those variations. This study shows that such "apparent" non-Coulomb sliding friction behavior can be attributed to a non-horizontal sliding trajectory due to the spatial variation of surface mechanical properties of the wood specimen. This mechanism seems to be plausible for most

Table 1
Values of the test variables for the reciprocating sliding friction test.

Tribometer variables	Value
Normal force [N]	30
Reciprocating frequency [Hz]	1
Stroke length [mm]	±2.85
Spring stiffness [N/mm]	10.19

of the tested cases, while for other ones, a more complex mechanism seems to be needed (not treated in this paper) to explain the observed variations. In the mechanical engineering literature, a non-horizontal sliding trajectory is often linked to what is called the wear-scar interaction [26,29,30] between a slider and the worn track profile. In connection to that, the study also shows the relevance of tracking and measuring the corresponding normal force fluctuations during each cycle, which allows to link the variation of the measured worn surface profile to the observed variation of the frictional forces, highlighting that the wear-scar interaction could be the possible governing factor of some of the observed friction force variation. Within this framework, an optimization procedure is proposed to post-process the measured hysteresis curves, and extract an optimal coefficient of friction able to represent the frictional property during reciprocating sliding. Finally, a comparison with more conventional methods such as the mean method, the energy-based based method [31], and the use of dynamic friction laws such as the LuGre model [32] is shown and discussed.

2. Material and experimental setup

2.1. Material: wood sample preparation and characterization

The tested wood specimens are made out of European beech wood (hardwood) and spruce (softwood). The wood samples are cut from dry wood panels into cubic blocks, and the sizes of the wood blocks are all 20 mm × 20 mm × 20 mm. After cutting from the original wood panels, the wood samples are stored in a controlled environmental room, with a temperature around 20 °C and a humidity level of approximately 60%. The surfaces of the beech and the spruce samples are shown in Fig. 1 and Fig. 2, respectively. The reciprocating friction tests were run on three surfaces for each wood sample, as indicated in Figs. 1 and 2. For each plane, two perpendicular sliding directions were tested. To identify the different runs, the labeling composed of wood species, test plane, and sliding directions was established as shown in Figs. 1–2. For example, the friction test on the RT plane of beech wood sample along the radial axis was named B-RT-R, where B stands for beech, RT indicates the plane and the last letter R defines the sliding direction along the radial axis.

On the RT plane of the beech wood sample (Figs. 1(a), (b)), there are horizontal and vertical darker lines across the whole surface. With reference to the wood anatomy terminology, the darker horizontal lines are formed by the latewood cells in trees, while the brighter regions in between include the earlywood cells [33]. Such latewood and earlywood cell regions are visible in the RT and in the RL planes for both beech and spruce samples. The darker vertical lines in Fig. 1(b) are the rays, which are composed of ray parenchyma cells [33]. The rays can also be seen on the TL plane in Fig. 1(d). On the RT plane (Fig. 2(b)) and RL plane (Fig. 2(c)) of the spruce sample, the dark brown lines are the latewood cell regions.

2.2. Experimental setup: tribometer and profilometer

The friction tests were conducted on the tribometer MFT-5000, developed by Rtec Instruments. Fig. 3 shows the assembled test setup, inclusive of the wood sample and the steel sphere. The wood specimen is clamped by two steel holders on top of the moving base of the
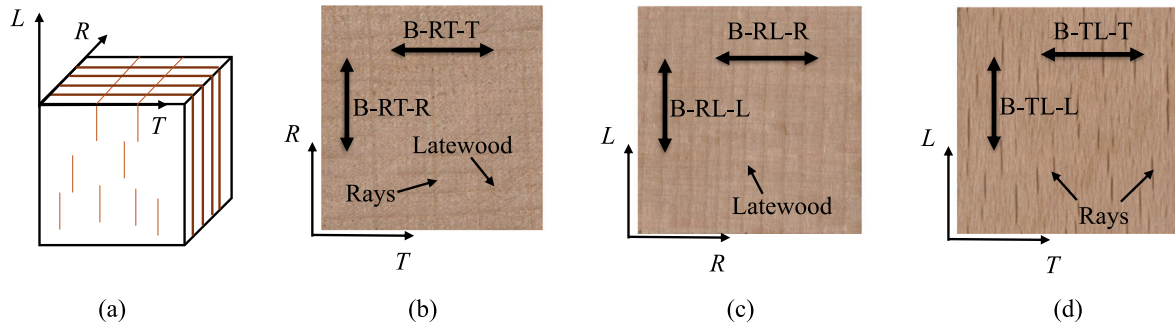
Fig. 1. Original surfaces of beech wood sample (Fagus sylvatica) before the friction test: (a) 3D schematic diagram of the beech sample; (b) radial–tangential plane; (c) radial–longitudinal plane; (d) tangential–longitudinal plane.
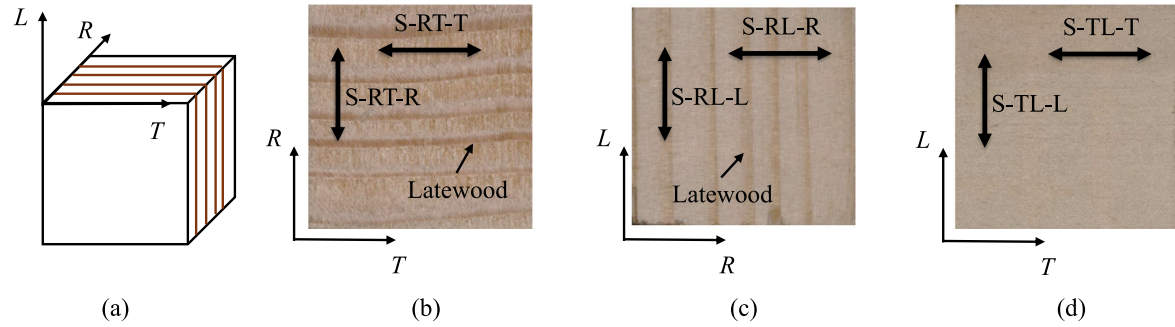

Fig. 2. Original surfaces of spruce wood sample (Picea abies) before the friction test: (a) 3D schematic diagram of the spruce sample; (b) radial–tangential plane; (c) radial–longitudinal plane; (d) tangential–longitudinal plane.

tribometer. In the application of steel-to-wood joints [11,15,18], plastic deformation of wood is widely observed and related to the friction behavior, thus the steel ball is selected as the counter specimen to penetrate the wood specimen, causing plastic deformation. One concern of using the steel ball as counter material is that the radius of the sphere needs to be large enough to eliminate microscale properties of wood. Therefore, a steel sphere with a radius of 3.25 mm is selected. Note that the radius is also dictated by the available rigid cylinder that acts as the holder, held by a leveled horizontal steel arm. The spring allows for a smooth transfer of eventual normal force variation during a reciprocating sliding test. To initiate the test, the upper casing hosting the normal load cell moves down, forcing the normal contact between the steel sphere and the wood sample, until the normal force reaches the set value. The feedback control system in the measurement device makes sure that during the sliding test, the amplitude of the normal force remains around the set value.

The schematic diagram of the applied forces in the test rig is shown in Fig. 4(a). After the normal force P reaches the set value, a sinusoidal horizontal displacement will be applied on the moving base, triggering the friction force between the steel sphere and the wood specimen. The friction force acting on the sphere is transmitted through the cylinder and the arm, which are designed to act as a rigid body and allow the friction force to be measured by a piezo-force sensor, mounted on the right end of the holding arm, as shown in Fig. 3(a). The resolution of the piezo-force sensor is 4.5 mN. The applied normal force is also measured by a piezo-force sensor, with a resolution of 15 mN. The horizontal displacement x of the moving base is measured by a linear variable displacement transducer (LVDT) mounted below the base. The chosen sampling frequency for all the tests was set as 2000 Hz and all tests were running for 10 min. The reciprocating frequency was set at 1 Hz which stays within the range of typical earthquake-induced dynamic loads on wood structures, and the maximum sliding stroke of the moving base for all test cases was set around ±2.85 mm. This adopted sliding distance makes sure that the steel sphere can run across more than one growth ring, covering latewood and earlywood regions.

The applied normal forces for all test cases were set at 30 N to cause obvious plastic deformation on two wood specimens. All the values of the test variable are listed in Table 1.

After the friction tests, the surface profile of the worn tracks was measured by a profilometer named VR-6200 produced by Keyence. The resolution of the camera was 0.0074 mm in both dimensions and the size of the measuring area was 1024 × 768 pixels.

3. Results of the reciprocating sliding friction tests

3.1. Friction and normal force measurements

Fig. 5 shows the envelopes of the friction force measurements, drawn by connecting the maximum measured peak (positive and negative) for each cycle, for beech and spruce, respectively. The measurement results are shown from the start of each test, hence they are all inclusive of the so-called running-in period [34], exhibiting significant variation in time for the initial cycles. For both wood species, after the initial running-in period, the amplitudes of the maximum measured horizontal forces slightly increase for an increasing number of cycles. After 599 cycles of reciprocating sliding, the maximum value of measured horizontal forces for two cases was still gradually increasing. Fig. 6 shows the envelopes of the measured normal forces, connecting the peaks in each cycle. During the first cycles, the normal force attempts to settle in due to the significant changes occurring on the sliding track. After the first minute of testing, the envelope of the amplitudes of the measured normal force remains within a stable range. With reference to the normal force, the largest range is provided by the test conducted on the RL plane, sliding along the radial direction (RL-R), for both beech and spruce samples. The spruce sample also shows a large variation along for the RT-R case, while a more reduced range was observed for beech. It is noted that the value of the largest variation range is less than 1 N for beech, and less than 2 N for spruce. In the next subsection, we will show that these variations are not able to fully explain the fluctuations in the friction force observed in the hysteresis
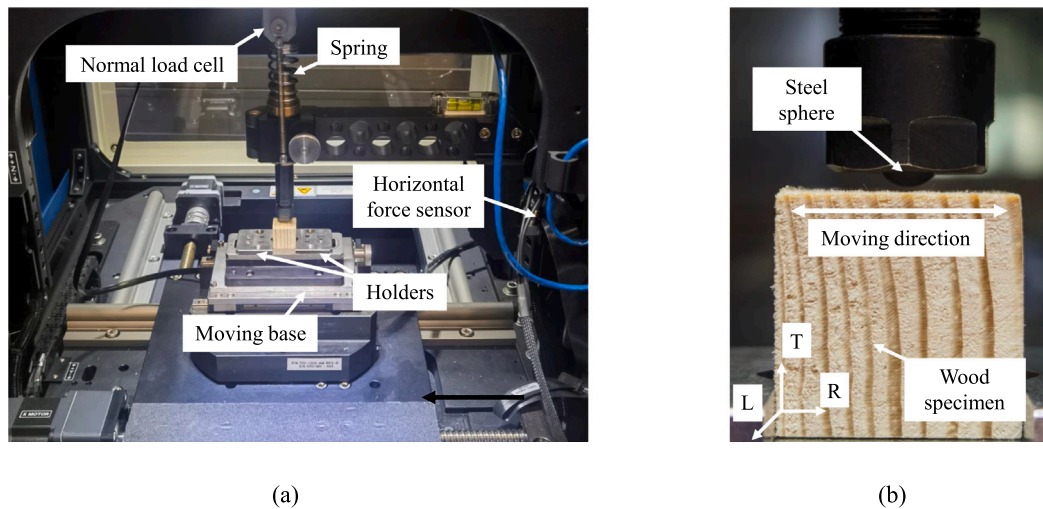
(a)

(b)

Fig. 3. Photos of the tribometer and the test setup: (a) overview of the test setup; (b) close view of the contact between the steel sphere and the wood sample in test case S-RL-R.
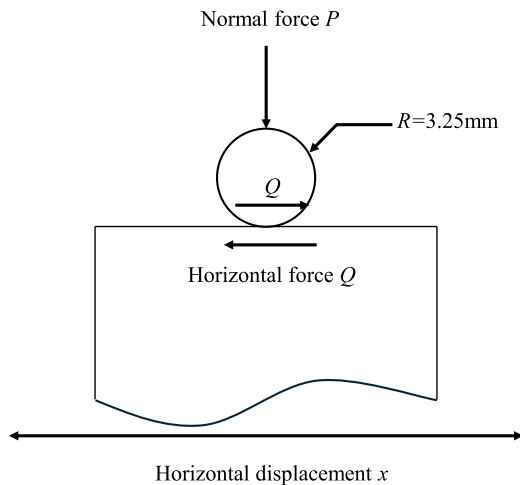

Fig. 4. Schematic diagram of the test setup and the tribometer.

curves. Whereas a smaller range is identified for the tests carried out for RT-T, RL-L and TL-L, for both wood species. The possible physical reasons for such differences in the observed range are discussed in the next section.

The friction hysteresis loops of the initial cycles and the last cycle for selected test cases are shown in Fig. 7. Note that only two types of hysteresis curves for each wood species are displayed, since they are representative of the two typical shapes encountered during all the tests. Each of the hysteresis curves can be divided into two phases: one phase includes the gross slip, during which the sliding speed increases up to the maximum value, and the other phase includes the stick and the partial slip, during which the sliding direction of the steel sphere reverses. Note that the slope of the latter phase is rather steep, for all the measured hysteresis curves, hence it is not possible to make a clear distinction between stick and partial slip phase. In the hysteresis loops, when the value of measured displacement increases, the sliding direction is defined as the forward direction, and when the displacement decreases, the sliding direction is marked as the reverse direction.

After the first reciprocating cycles (running-in period), the hysteresis loops in all test cases reach a "steady-state" behavior, exhibiting similar shapes to the last one, despite the increase of cycles. While the shape of the hysteresis curves for each cycle remains rather similar,

the only detectable difference, as shown in Fig. 5, consists in a slight increase of the maximum amplitudes, for increasing cycles. These amplitude peaks either occur at the point of velocity reversal (see Fig. 7(a), (c)), or during sliding (see Fig. 7(b), (d)). While approaching the end of the sliding stroke (deceleration phase), the so-called "hook-like" feature was observed, a typical experimental outcome reported in fretting friction test of metals [26]. The hook-like feature consists of an increase in the friction force, while approaching the end of the sliding stroke, as shown in Fig. 7(a), (c) (and also in Fig. 7(b), (d), even though less pronounced). With reference to the fluctuations observed during gross slip, case B-RT-R (Fig. 7(b)) and S-RT-R (Fig. 7(d)), we found that the number of peaks in the measured horizontal force on beech wood is higher than the number of peaks in spruce. However, the fluctuation observed for the spruce specimen (Fig. 7(d)) is generally larger than the one provided by the beech specimen (Fig. 7(b)). It is worth highlighting that the absolute value of the measured horizontal forces at the same location for the two opposite sliding directions is different. The aforementioned hook-like feature, the fluctuations observed during sliding, and the lack of repeatability in terms of absolute values between the forward and reverse direction, may indicate a typical non-Coulomb friction behavior. It is worth highlighting that in case the Amonton–Coulomb linear proportionality between the friction force and the normal force would be obeyed, the hysteresis loops would be symmetric with respect to the horizontal axis, meaning that the friction force variation is entirely due to the normal force variation.

Figs. 7(e), (f), compare the normal force variation and the horizontal force variation, measured during the gross slip phase of the 599th cycle, for case B-RT-R and S-RT-R. Results show that for both cases, the location of the peaks of the measured horizontal force do not align with the peaks observed in the normal force. This indicates that the normal force variation is not the predominant factor causing the variation in the measured horizontal force, if the Amonton–Coulomb proportionality would be assumed. Moreover, the variation in the measured normal force (around 0.5 N for case B-RT-R and 1.5 N for case S-RT-R) is much smaller than that of the measured horizontal force (around 2 N for case B-RT-R and 10 N for case S-RT-R). Based on this comparison, we can infer that there are other factors influencing the measured horizontal force apart from the normal force.

3.2. Relationship between surface profile and normal displacement of the steel sphere

We will demonstrate in this section, that the large fluctuations during gross slip observed, for example, in Figs. 7(b), (d), mainly originate from the alternation of earlywood and latewood cell regions,
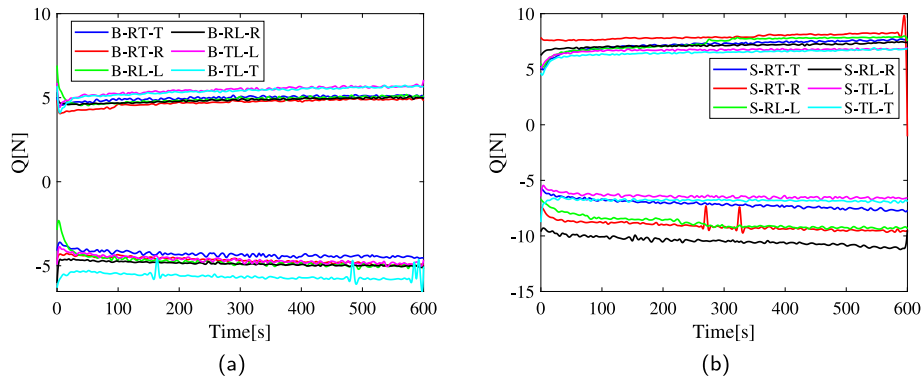
Fig. 5. Envelopes of the measured horizontal force on two samples: (a) beech wood; (b) spruce wood. Note that the mean normal force was set to 30 N, for all measurements.
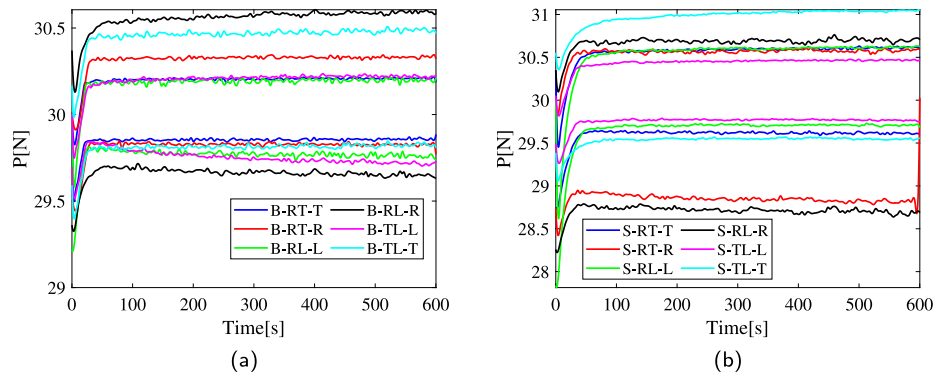

Fig. 6. Envelopes of the measured vertical force for two samples: (a) beech wood; (b) spruce wood.

during the sliding between the steel sphere and the wood specimen. In Section 4, it will be shown that this alternation will cause an inclination of the actual friction and normal force, due to intrinsic differences in terms of density and mechanical properties between the earlywood and latewood cell regions. This spatial variation of the mechanical properties will inevitably influence the wear behavior of the wood specimen during sliding. To investigate the worn track, the wood specimen profile was measured by a profilometer. The surface profile of worn tracks for test cases B-RT-R and S-RT-R are shown in Figs. 8(a)–(b), respectively. According to [35], the hardness of earlywood and latewood is different, thus the wear depth of the two components changes. While smaller variations in terms of depths are observed for the beech wood specimen, the worn surface profile for spruce is rather uneven. To refine the analysis, a detailed profile over one line (see dash-dotted black line in Figs. 8(a)–(b)), that crosses the center of the worn tracks, is taken out. The extracted longitudinal profile of the worn track is then compared with the estimated relative normal displacement of the steel sphere, see Figs. 8(c)–(d). It is noted that the two curves were manually shifted to make them comparable. The relative normal displacement, indicated by the line, was calculated by dividing the measured normal force (P) with the stiffness of spring (S_{spring}, see Table 1 for the adopted value). By comparing the images of the worn tracks, with the measured roughness and estimated displacement, it is clear that whenever the earlywood cell region is crossed, a dip appears in the measured roughness profile and the estimated normal displacement. However, whenever the latewood is approached, there is a peak in the relative normal displacement, and a reduced depth in the roughness profile can be observed.

For case B-RT-R (see Fig. 8(c)), the magnitude of the displacement of the spring is comparable with that of the line profile of the worn track, yet the position of the peaks does not fit exactly with the peaks on the line profile. For case S-RT-R (see Fig. 8(d)), both the magnitude and the position of the peaks in the displacement of the spring fit with those of

the line profile. However, the match between the surface profile and the deformation of the spring does not hold in all test cases, see Appendix for the comparison results for all test cases.

The relationship between earlywood, latewood and normal displacements also explains why some of the envelopes of the measured normal forces for beech and spruce show large differences between them, see Fig. 6. In test cases S-RT-R and RL-R (the latter for both beech and spruce), the steel sphere ran across both the earlywood and latewood regions. The difference in hardness and density between these two regions, caused larger normal displacements and therefore larger variation in the measured normal force. It was also noted that for RT-R test cases, the beech specimen showed a smaller variation in the measured normal force, compared to the spruce specimen. Since the RT plane provides the highest resistance to normal loads, the observed difference can be explained by the higher hardness property of beech wood, if compared to spruce. Large variation were also observed on tests carried out over the RL plane, which is generally the weakest plane for indentation-like loads. The latter holds true for both beech and spruce specimens.

4. Method: an optimization framework to post-process the experimental data

Based on the analysis in Section 3, the variation of the normal force seems to be related to the worn surface profile and its varying mechanical properties, resulting in normal displacements of the steel sphere during the sliding phase. Fig. 8 showed that the presence of small regions characterized by a higher density of fibers (e.g. latewood or rays), may cause an interference during sliding due to an attempt of local interlocking, causing the presence of peaks and troughs on the worn surfaces. This can inevitably lead to hysteresis curves exhibiting an apparent non-Coulomb friction behavior. However, before challenging Coulomb's law, an attempt can be made to quantitatively
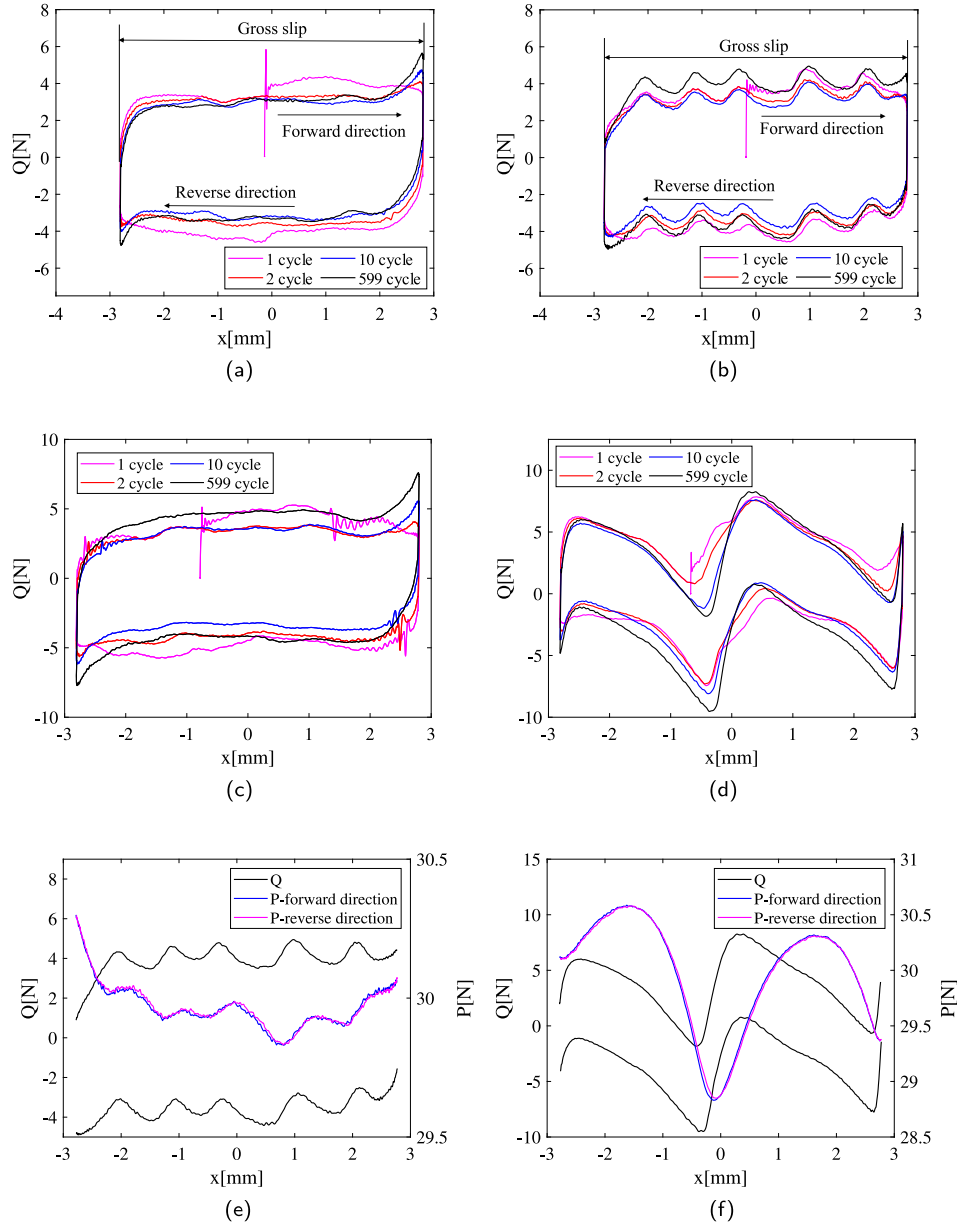
Fig. 7. Hysteresis loops of measured horizontal forces and sliding displacement for selected test cases: (a) B-TL-L; (b) B-RT-R; (c) S-RT-T; (d) S-RT-R; (e) comparison between the horizontal force and the normal force in the gross slip phase of the 599th cycle for case B-RT-R; (f) comparison between the horizontal force and the normal force in the gross slip phase of the 599th cycle for case S-RT-R.

explain the observed variation through the non-uniform worn track, which can lead to local inclinations of the sliding direction [26,29,30]. Such inclinations, due to the wear–scar interaction between the two sliding surfaces, will result in deviations between the actual friction force and the measured one. Therefore, the following analysis assumes that the measured hysteresis curves observed throughout this study can also be explained by the wear–scar interaction mechanism [26]. In this section, an optimization framework is proposed to post-process the experimental data by taking into account the effect of a worn profile and the resulting variations of the normal displacements.

4.1. Formulation of wear scar interaction the theory

A possible free body diagram showcasing the forces and their orientation of the steel sphere in contact with the wood specimen, in case the wear-scar interaction mechanism holds, is shown in Fig. 9. The wear-scar mechanism, as explained in [26], causes an inclined surface, and

the sliding direction follows a curvilinear trajectory during the friction test. Hence, the balance of forces applied on the steel sphere leads to the following equations in the horizontal and vertical direction (excluding inertial forces):

$$\frac{k(x)N(x)}{\sqrt{1 + k(x)^2}} + \text{sgn}(\dot{x})\frac{\mu N(x)}{\sqrt{1 + k(x)^2}} = Q(x), \tag{1}$$

$$\frac{N(x)}{\sqrt{1 + k(x)^2}} - \text{sgn}(\dot{x})\frac{\mu N(x)k(x)}{\sqrt{1 + k(x)^2}} = P(x), \tag{2}$$

$$k(x) = \tan\theta = \frac{\partial f(x)}{\partial x}, \tag{3}$$

where k is the local slope of the curvilinear trajectory of the steel sphere, N is the actual normal force which is perpendicular to the sliding trajectory, $f(x)$ is the curvilinear trajectory (or sliding path), x indicates the horizontal coordinate (or position) of the steel sphere, and $\dot{x}$ is the sliding velocity of the bottom moving plate. Eqs. (1)–(2) implies the existence of small angles (or slopes), since the wear-scar hypothesis
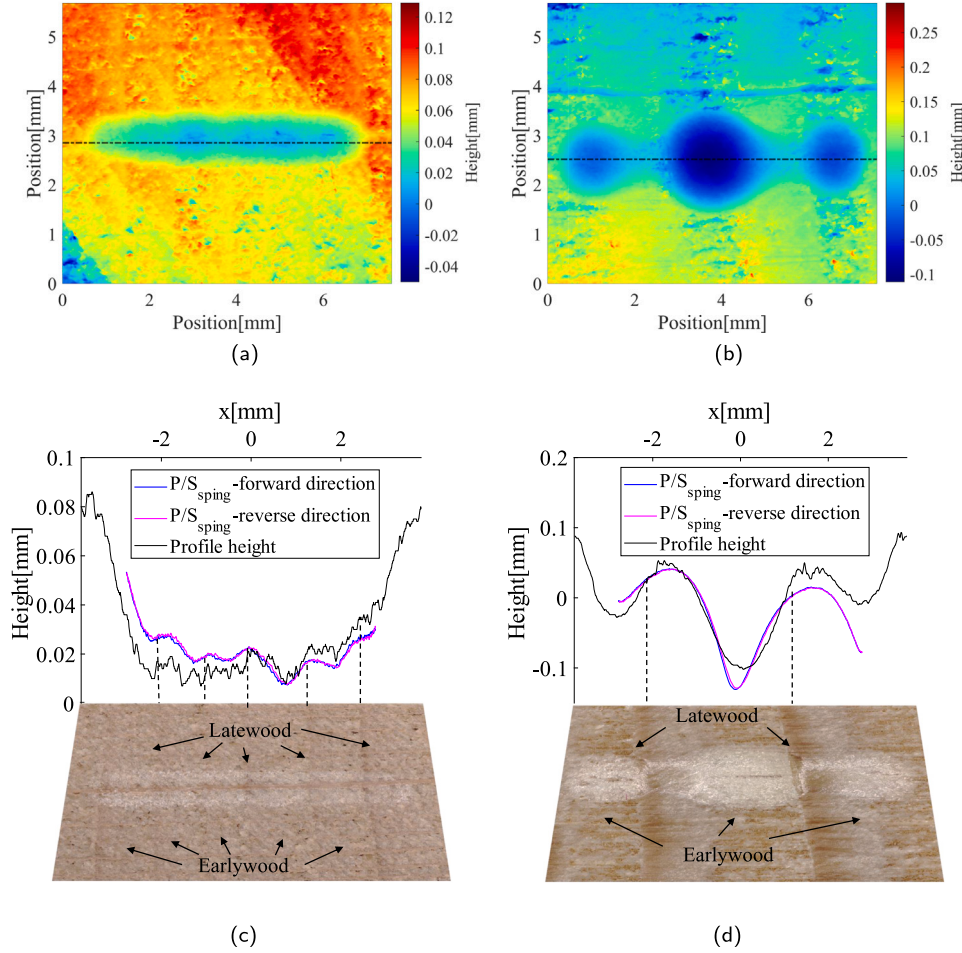
Fig. 8. Comparison of the line profile height and the relative deformation of the spring: (a) surface profile of the worn area for case B-RT-R; (b) surface profile of the worn area for case S-RT-R; (c) comparison results between the surface worn profile and the normal displacements (for both direction) for case B-RT-R; (d) comparison results between the surface worn profile and the normal displacements (for both direction) for case S-RT-R.
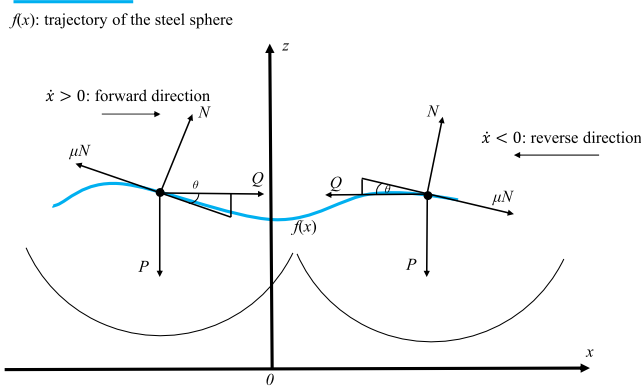
Fig. 9. Schematic diagrams of the influence of sliding trajectory geometry on the friction measurements.

falls down for high slope angles during sliding (see [30]). Note that for $k = 0$ (neglecting the inclination), Eqs. (1)–(2) naturally leads to the Amonton-Coulomb's law. To effectively know the actual sliding path ($f(x)$) is rather challenging, since sensors cannot be placed at the interface to measure the tiny displacements in the normal direction. However, it has been shown before, that it is possible to link the normal force variation to the normal displacement of the contacting steel sphere, by dividing the normal force with the given stiffness value

of the upper spring. Note that depending on the choice of the spring stiffness, the worn profile of the wood specimen may look different. When a much harder spring is applied, a flatter wear profile might be formed and the observed friction hysteresis loops could have different features. However, the choice of a softer spring, allows to introduce a control variable in the process, as long the chosen spring stiffness is smaller than the wood specimen stiffness. Therefore, $\partial f(x)$ could be approximated through the displacement of the spring, which reads as follows:

$$\partial f(x) \approx df(x) = (f_{i+2}(x) - f_i(x)) = \frac{P_{i+2}(x) - P_i(x)}{S_{spring}}, \tag{4}$$

from which $k(x)$ can be obtained by differentiating $f(x)$ as follows:

$$\frac{\partial f_{i+1}(x)}{\partial x} \approx \frac{f_{i+2}(x) - f_i(x)}{x_{i+2} - x_i} = \frac{1}{S_{spring}} \frac{P_{i+2}(x) - P_i(x)}{x_{i+2} - x_i}. \tag{5}$$

It is noted that in Eq. (5) the differentiation procedure was conducted for every three data points of the measured normal force and displacement, hence $\frac{\partial f_{i+1}(x)}{\partial x}$ is obtained on all the corresponding time points in the experiment except for the first and last one. The tribometer measurements directly provide $Q(x)$, $P(x)$ and x, and $k(x)$ can be obtained according to Eq. (5). Thus, in Eq. (1) and (2), only μ and $N(x)$ are the unknowns. Since the force analysis in Fig. 9 holds in the gross slip phase as indicated in Fig. 7, only the experimental data obtained during the gross slip are used for the following analysis. To identify the optimal sliding friction coefficient $\hat{\mu}$, an optimization procedure is used by minimizing the error between the measured and predicted (or corrected) horizontal force, accounting for the effects of the geometry

of the worn profile. For each reciprocating cycle, and with reference to the gross slip phase, the following cost function is minimized:

$$\hat{\mu} = \underset{\mu}{\arg\min} J \quad \text{where}$$

$$J = \frac{|Q_m^{\text{forward}} - Q_w^{\text{forward}}|}{|Q_m^{\text{forward}}|} + \frac{|Q_m^{\text{reverse}} - Q_w^{\text{reverse}}|}{|Q_m^{\text{reverse}}|} \tag{6}$$

where Q_m^{forward} and Q_m^{reverse} are the measured horizontal forces for the forward and reverse gross slip phase, respectively. Whereas Q_w^{forward} and Q_w^{reverse} represent the predicted horizontal force for the gross slip phase of the two directions, and $||$ represents the 2-norm of the vector. In the optimization procedure for each sliding cycle, at first, the actual normal force $N(x)$ is determined by Eq. (2), by providing the slope of the trajectory $k(x)$, the measured normal force $P(x)$ and a trial value of the coefficient μ. Then, the horizontal force $Q(x)$ is obtained by Eq. (1). This process is conducted iteratively until the minimum of the cost function J is found with an optimal COF. The optimization function *f minsearch* in MATLAB was used to implement this optimization procedure.

4.2. Application of the proposed framework

To illustrate the hypothesis of the wear-scar interaction influence on the variation of the measured frictional forces, the proposed optimization procedure was applied to find the optimal $\hat{\mu}$ for the 599th cycle of test cases B-RT-R and S-RT-R. Since the numerical differentiation in Eq. (5) is very sensitive to the measurement noise, a moving average filter was used to process the measured normal force variation, in which the window size is set as 10. This particular window size value is large enough to get a smooth $k(x)$ for this sampling frequency (2000 Hz) while keeping the significant varying features in the measured normal force. The estimated slope of the sliding trajectories for the 599th cycle of test cases B-RT-R and S-RT-R is shown in Fig. 10. The difference between the sliding slope for the two sliding directions is very small for both cases. Although the measured normal force was filtered, there is still numerical noise due to the differentiation process present in k. Fig. 11 also shows the behavior of the cost function indicated in Eq. (6). The values of the cost function, shown for a varying μ between 0 and 1, show clear minima for both specimens around 0.12. Specifically, the results of the optimization procedure highlight that the optimal values of μ for the 599th cycle of test cases B-RT-R and S-RT-R. are rather similar, 0.122 and 0.124, respectively.

By taking into account the wear-scar interaction hypothesis, it is possible to reproduce the measured friction force, after identifying $\hat{\mu}$. Fig. 12 shows the corresponding predicted horizontal forces for the 599th cycle of test cases B-RT-R and S-RT-R, comparing it with the measured ones. Fig. 12 indicates that the large variations in the horizontal forces can be successfully reconstructed by the proposed procedure and the main factor causing the fluctuations in the measured friction force is the wear-scar interaction effect, leading to inclined friction and normal forces. However, there is still a small amount of high-frequency fluctuations in the predicted horizontal forces, which may be caused by the noise introduced through the numerical differentiation used to compute the slope of the sliding trajectories, as shown in Fig. 10. The results show that by considering the influence of the wear-scar interaction, a constant coefficient of friction can explain the observed sliding friction behavior.

The optimization process was then applied to all cycles of all test cases. The obtained evolution over successive cycles of the identified optimal coefficient of friction, for all test cases on beech and spruce wood, is shown in Fig. 13. The corresponding cost function value J for different test cases and for each cycle is shown in Fig. 14. For beech wood, see Fig. 13(a), the results show that there are sharp changes in the coefficient of friction for the first cycles, observable in all test cases and that the friction coefficient (after the running-in period) is slowly increasing as the number of reciprocating cycles increases. After

the running-in period, the friction coefficients for all test cases range between 0.1 and 0.12, approximately. For test case B-RL-L and B-TL-T, the coefficients of friction are nearly the same. The cost function value J in Fig. 14(a) shows that besides test cases B-RL-L and B-TL-T, the residual error between the simulated and measured friction hysteresis cycles is below 0.4, including the running-in cycles, which represents a good fit of the friction hysteresis cycles as shown in Figs. 12(a), (b), for which the cost function J was equal to 0.3085 and 0.3748, respectively. For test cases B-RL-L and B-TL-T, the cost function value J is quite large for the running-in cycles, while for the successive cycles the value also decreases below 0.4. The reason for the large value of J in running-in cycles could be that, for those two cases, the sliding plane and direction were significantly deformable. Therefore, in case of significant surface deformation, the variation in the measured normal force is not only influenced by the normal displacement of the steel sphere due to wear-scar interaction, but also by the deformation component of the wood plane (the latter could be larger than the spring stiffness). With reference to the Bowden and Tabor theory of friction, this would call for the presence of the so-called hysteretic component (linked to surface deformation) to explain the observed friction force variation. The mismatch between the trend of the estimated normal displacements and the filtered line profile of the worn surface will cause larger errors in the estimation of k, obtained by Eqs. (4) and (5), causing larger cost function values for those cycles.

Substantial changes in the coefficient of friction for the first cycles, can also be observed for spruce wood, see Fig. 13(b). The time evolution of the friction coefficient for spruce also shows a larger scattering of the results, ranging from 0.08 to 0.16. For test cases S-RT-T and S-RT-R, the coefficients of friction are constantly increasing as the number of sliding cycles increases. For test cases S-RL-L, S-TL-L and S-TL-T, the friction coefficients are rather steady after the first 300 cycles. As for test case S-RL-R, the coefficients of friction stay around 0.09 until the first 500 cycles, followed by a slight increase up to 0.095, after 500 cycles. The cost function value J for the running-in cycles of all test cases on spruce is larger compared to the subsequent cycles. As explained before, a rather softer surface could cause a large error in the obtained k, thus for spruce (a much softer wood compared to beech wood), the running-in phase lasts generally longer, until the deformed worn track gets stiff enough. For the test case S-RL-R, the residual error is always large despite the number of cycles, and only the number of peaks in the gross slip phase of friction hysteresis cycles can still be captured by the wear-scar interaction theory, while the magnitude of the variation cannot be determined. In Appendix, the possible reason for the large cost function error will be discussed.

It is noted that the sliding COF obtained in this study ranges from 0.06 to 0.13 for beech and 0.08 to 0.16 for spruce, which is much lower than the reported COF between steel and dry balsam wood (0.5) [18], steel and wenge (around 0.6) and tamarisk (0.2–0.7) [36], and steel and spruce (0.5) [25]. However, it seems to fit within the range of the COF reported in [20,21]. Besides the influences of environmental conditions and the moisture content of wood, the low sliding COF measured in this study between wood and steel might be due to the stiffer and harder worn track on the wood surface, which caused a smaller deformation term (hysteresis friction term according to the Bowden and Tabor theory of friction) over subsequent cycles.

An alternative method to obtain the COF from friction hysteresis cycles is the energy-based method, which is based on a dissipated energy equivalence and was proposed to reduce the influence of the ploughing effect in calculating the coefficient of friction in fretting wear [37]. The energy-based friction coefficient is defined as the ratio between the actual measured dissipated energy within the hysteresis cycle and the energy that would be dissipated if the hysteresis curve is governed by a Coulomb friction behavior. The energy-based coefficient of friction reads as follows:
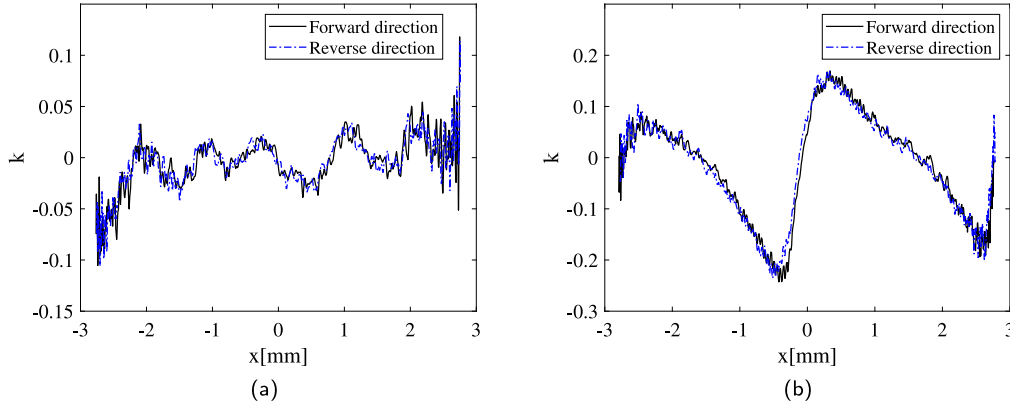
$$\mu_{Ed} = \frac{E_d}{4P\delta_{max}} \tag{7}$$

Fig. 10. Spatial variation of the slope k of the sliding trajectory: (a) test case B-RT-R and (b) test case S-RT-R.
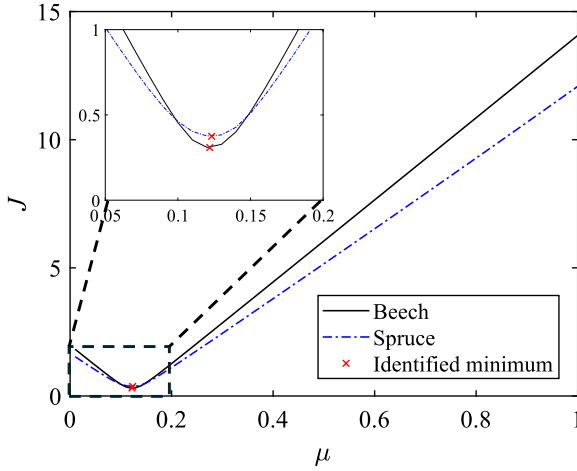

Fig. 11. Behavior of the cost function J for a varying μ, for the 599th cycle of test case B-RT-R and S-RT-R.

where E_d is the dissipated energy represented by the area of the hysteresis friction cycle, P is the applied normal force, and its value is given as the average normal force estimated during the two sliding phases of each hysteresis cycle, and δ_{max} is the maximum gross slip displacement. The COFs obtained by the energy-based method for test cases on beech and spruce are shown in Fig. 15. Results show that for all test cases, there are obvious drops in the obtained energy-based COF of the first cycles, which are different from some of the increasing trends shown in the optimized COFs for the first cycles in test cases B-RL-L, B-TL-T and S-TL-T. For most of the cases, the COFs obtained by those two methods are rather similar, except for test case S-RL-R, a quantified comparison will be presented in the next section.

5. Comparisons and discussion

5.1. Comparison on the mean method and the energy-based method to obtain the COF

Besides the adopted method based on the wear-scar interaction, it is worth comparing the identified optimal $\hat{\mu}$ with coefficients of friction determined through alternative methods, see [31] for a detailed discussion. A standard one refers to the mean coefficient of friction μ_{av}, in which the absolute value of the sliding friction force is averaged and divided by the normal force within each cycle. The other one is the energy-based COF as described before. The results of both methods are compared with the identified friction coefficient through the wear-scar interaction method as shown through error bar plots in Fig. 16. The

error bar contains the statistics obtained by the error estimated by the difference between the optimal friction coefficient (used as reference), and the one calculated through the mean method (Fig. 16(a)) and the energy-based method (Fig. 16(b)), for each test cycle. Results show that the difference between the COF obtained by the mean method and by the optimization process ($\hat{\mu}$) is very small, except in test case S-RL-R, as shown in Fig. 16(a). For test cases B-RL-L and B-TL-T, the large variances are due to the difference between the COF obtained in the running-in cycles. A similar difference between the COF obtained by the energy-based method is also found in Fig. 16(b), as a large difference exists in test case S-RL-R, and large variances can be observed for test case B-RL-L and B-TL-T. Results show that in most test cases on measuring the friction force between wood and steel, it is reasonable to utilize the mean method or energy-based method to obtain the actual sliding COF, provided that the variation in the friction hysteresis curves can be explained by the wear-scar interaction theory. However, for test case S-RL-R, there is a relatively large error in the cost function, and the COFs obtained by the three methods are also different. For this case, it seems rather difficult to determine which COF can be considered as the reference one, as the friction hysteresis curves cannot be fully explained by the wear-scar interaction theory.

5.2. Critical view on the application of dynamic friction laws

As indicated previously, test cases S-TL-T, RT-T, RL-L, TL-L for both beech and spruce, are not characterized by significant fluctuations during the gross slip phase. However, whenever velocities decrease to zero, there is a clear increase of the friction force, reaching a peak as the bottom plate stops before a velocity reversal. An example of such curves is shown again in Fig. 17, which refers to test case S-RT-T. It is rather tempting to fit hysteresis curves such as these, by dynamic friction models, which depend on several state variables governed by a respective state evolution law. Examples of such models are represented by the Bouc-Wen model [38], or the LuGre [32] model, just to name a few. The LuGre model will be used to attempt a fit, which reads as follows:

$$F = \sigma_0 z + \sigma_1 \dot{z} + \sigma_2 v \tag{8}$$

$$\dot{z} = v - \frac{\sigma_0 |v|}{s(v)} z \tag{9}$$

where

$$s(v) = F_c + (F_s - F_k)\exp(-(v/v_s)^2) \tag{10}$$

in which v_s is the Stribeck's velocity, $F_s = \mu_S N$ and $F_k = \mu_k N$ are the static friction force and the kinetic friction force, respectively. Parameters σ_0, σ_1 and σ_2 are a stiffness and two damping coefficients,
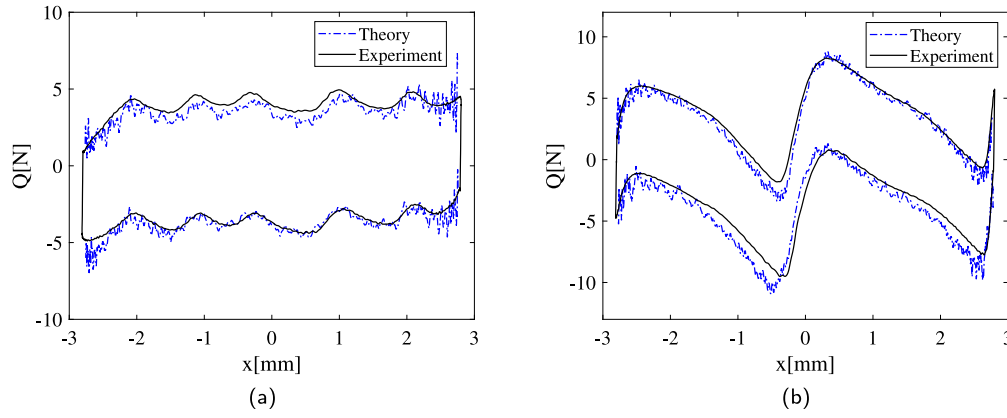
Fig. 12. Comparison between the horizontal force predicted by the wear-scar interaction theory (blue line) and the measurements for test case: (a) B-RT-R and (b) S-RT-R.
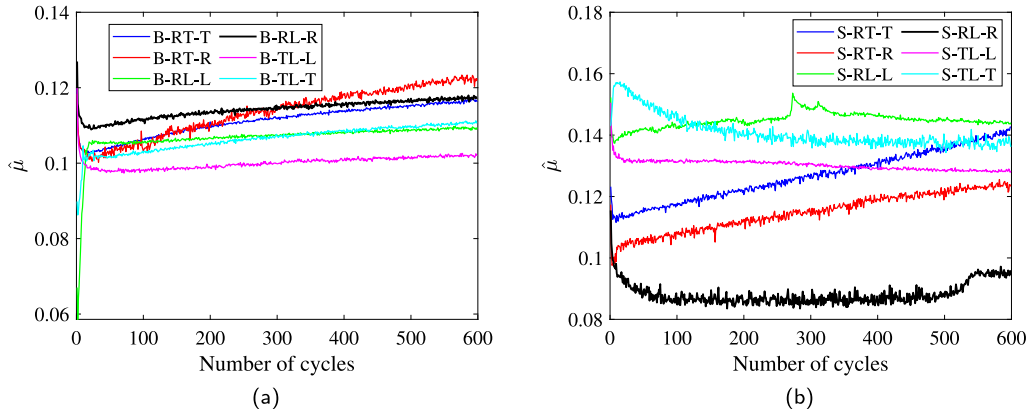

Fig. 13. Identified optimal coefficients of friction obtained by the wear-scar interaction theory for all test cases for (a) beech wood and (b) spruce wood.
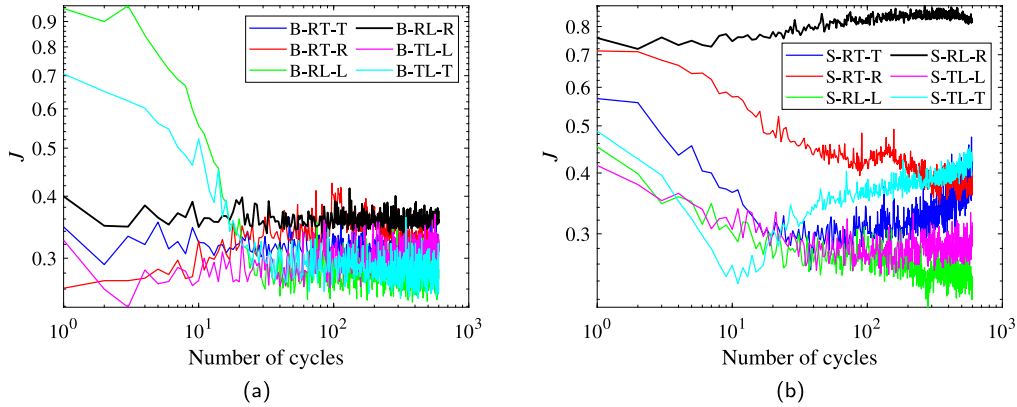

Fig. 14. Cost function value J utilizing the optimal COF($\hat{\mu}$) in different test cases on wood samples: (a) beech wood; (b) spruce wood.

respectively. According to the measured horizontal force in test case S-RT-T, F_c and F_s are set as 4.4 N and 8 N, respectively, while the other parameters are optimized according to the following cost function:

$$\hat{\sigma}_0, \hat{\sigma}_1, \hat{\sigma}_2, \hat{v}_s = \underset{\sigma_0,\sigma_1,\sigma_2,v_s}{\arg\min} J \quad \text{where}$$
$$J = \frac{|Q_m - Q_{\text{Lugre}}|}{|Q_m|} \quad (11)$$

where Q_m is the measured horizontal force in the 599th cycle of test case S-RT-T, and Q_{Lugre} is the predicted horizontal force by the LuGre model. By utilizing the MATLAB optimization function f minsearch, the identified minimum is found for $\sigma_0 = 31.6$ N/mm, $\sigma_1 = 0.001$ Ns/mm, $\sigma_2 = -0.005$ Ns/mm and $v_s = 8.09$ mm/s. The fitting result is compared

in Fig. 17, together with the predicted friction force through the wear-scar optimization method. The results show that both methods are able to simulate the friction force increase for decreasing values of velocities. However, the LuGre model allows such prediction only through a negative value of the parameter of σ_2, which indicates a negative damping effect. Since the increase in the friction force is only present at one side of the hysteresis curve (whenever a deceleration occurs, approaching zero velocity), it is very unlikely that a negative damping effect, usually linked to a frictional-weakening behavior often present at low velocities, can be attributed to the "hook-like" feature. In fact, the LuGre model predicts a similar friction force variation at the opposite extreme (as soon as the transition to gross slip occurs), whereas the measured hysteresis curve shows a smooth transition
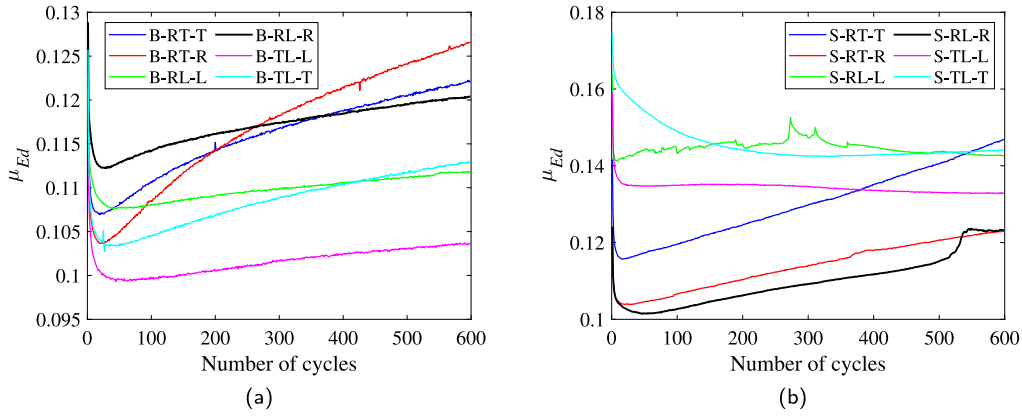
Fig. 15. Coefficients of friction obtained by the energy-based method for test cases on (a) beech wood and (b) spruce wood.
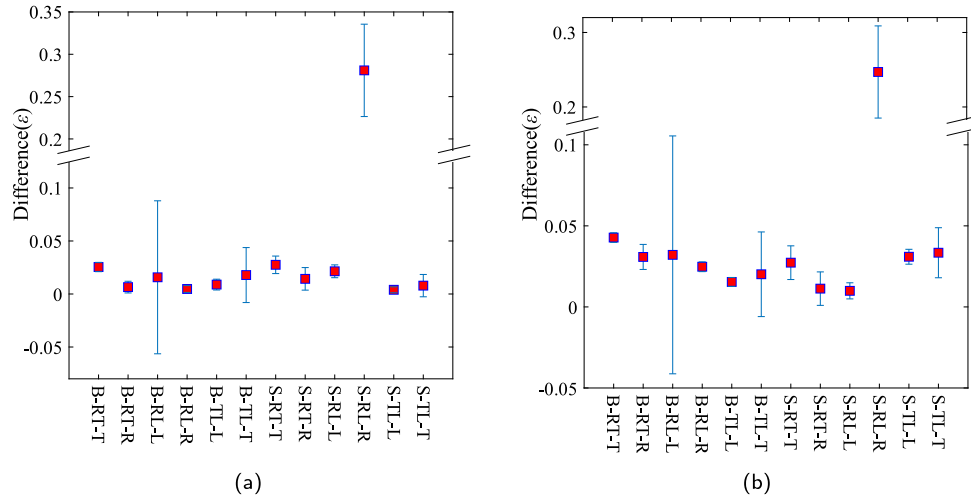

Fig. 16. Differences (ε) between the sliding COF obtained by the mean method, energy-based method and the optimization method used as reference (provided by Eqs. (1) and (2)): (a) mean method; (b) energy-based method.

from stick to slip. Therefore, it is worth underlining that even though dynamic friction laws are rather flexible to fit a plethora of hysteresis curves and are needed for specific forcing conditions, material pairs and to regularize friction discontinuities at velocity reversal points [39,40], attention should be paid to first pin down all the possible mechanisms that could alter the friction force during sliding. In this study, it was shown that, under specific conditions, the friction hysteresis curves can be explained by the wear-scar interaction whenever the magnitude of the normal displacement variation during reciprocating sliding is comparable to the "waviness" variation of worn track profile.

6. Conclusion

In this paper, reciprocating friction tests between a steel sphere and two species of wood, beech and spruce, were conducted by using a tribometer. The testing variables were the three different planes of the wood specimens, two perpendicular sliding directions for each plane. The sliding distance, the reciprocating frequency and the normal force were fixed. The tested surface were scanned through a profilometer to characterize the roughness and waviness of the worn profile. The hysteresis curves showcasing the friction force and the corresponding sliding displacement, obtained by the reciprocating sliding tests, showed fluctuations for the friction force and the normal force. Most of the measured normal force variation exhibited an excellent correlation with the worn profile, indicating a wear-scar interaction as the root-cause of the friction force variation.
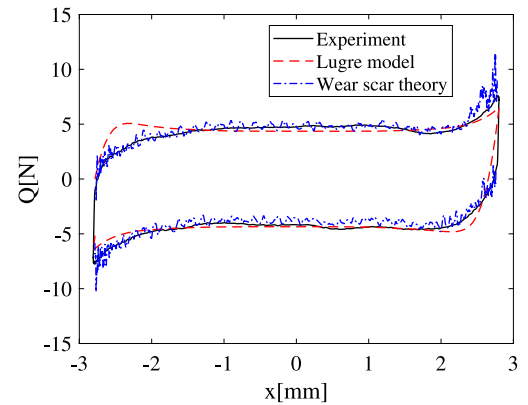

Fig. 17. Comparison of the optimization procedure considering the wear-scar interaction (blue dash-dotted line) and the LuGre model (red dashed line) for the 599th cycle of test case S-RT-T. The measurement is indicated through the continuous black line.

An optimization framework was then proposed for post-processing the experimental data, by taking into account the wear-scar interaction. Applications of the optimization framework on the tested cases showed that the apparent non-Coulomb friction hysteresis phenomena can be explained by the wear-scar interaction mechanism. It also enables to identify an optimal coefficient of friction representative of the gross slip
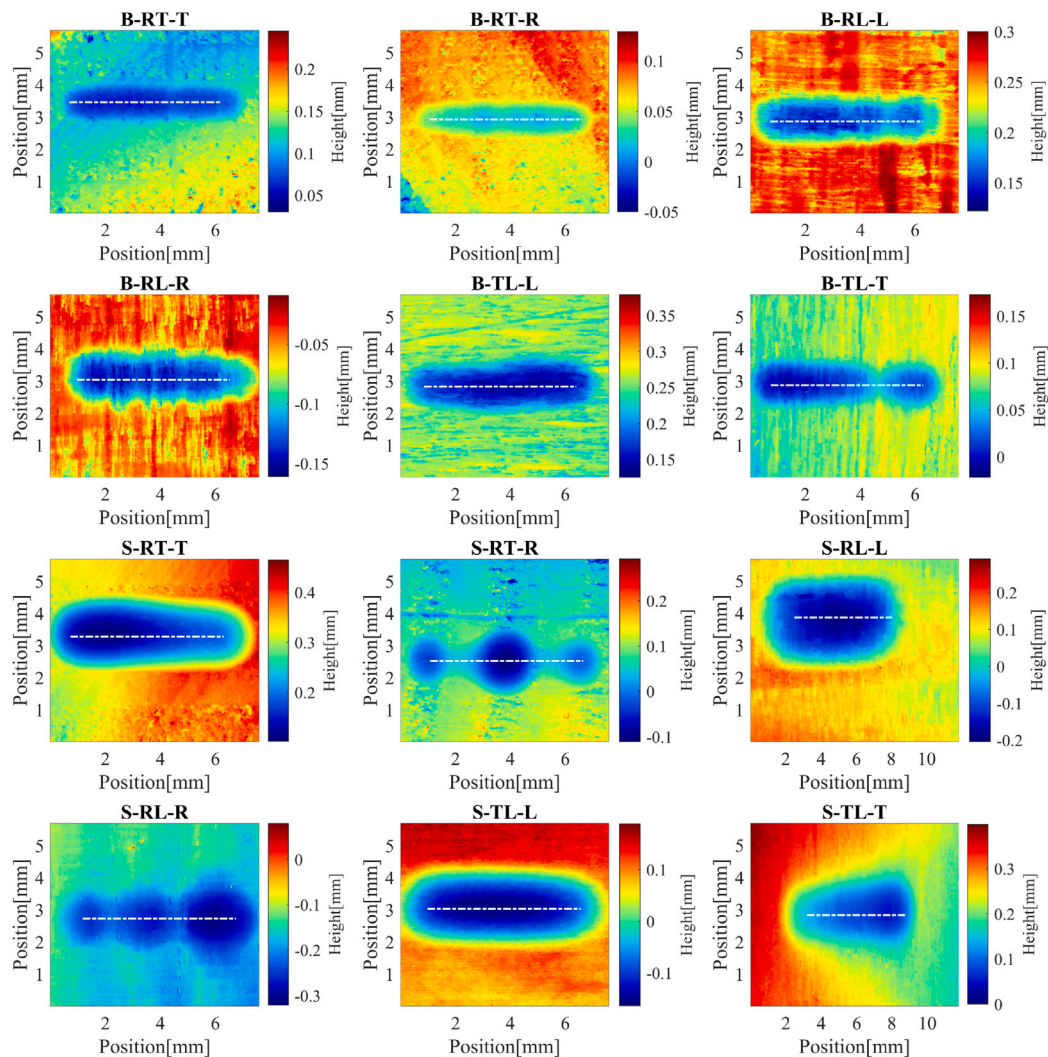
Fig. A.1. Surface profile of the worn area in all test cases.

phase. The results highlighted that the coefficients of friction between the test cases shown in Fig. 1 of beech wood samples were rather similar (see Fig. 13(a)), while the friction coefficients of spruce wood were characterized by larger differences (see Fig. 13(b)) among the various test cases displayed in Fig. 2. However, for test cases characterized by a more deformable wood plane, the wear-scar interaction is not a sufficient mechanism to fully explain the observed friction force variation.

Comparative studies between the results obtained through the wear-scar interaction and other methods to obtain friction coefficients were conducted. Besides few test cases, the results showed that the mean and the energy-based coefficient of friction were rather similar to the identified optimal coefficient of friction obtained through the wear-scar interaction method. This study shows that when processing the results of reciprocating friction tests, influenced by a high spatial variability of the mechanical properties, it is important to track and measure the worn surface profile and assess whether the measured normal displacements are comparable with the waviness of the profile. If so, and if the behavior of the friction force fluctuation is the same during the gross slip phase, the observed non-Coulomb sliding friction behavior can be explained by the wear-scar interaction model.

CRediT authorship contribution statement

Yi Zheng: Writing – original draft, Visualization, Validation, Methodology, Investigation, Formal analysis, Data curation, Conceptualization.

Alessandro Cabboi: Writing – original draft, Writing – review & editing, Investigation, Supervision, Methodology, Conceptualization.
Jan-Willem van de Kuilen: Writing – review & editing, Supervision, Conceptualization.

Declaration of competing interest

The authors declare that they have no known competing financial interests or personal relationships that could have appeared to influence the work reported in this paper.

Data availability

Data will be made available on request.
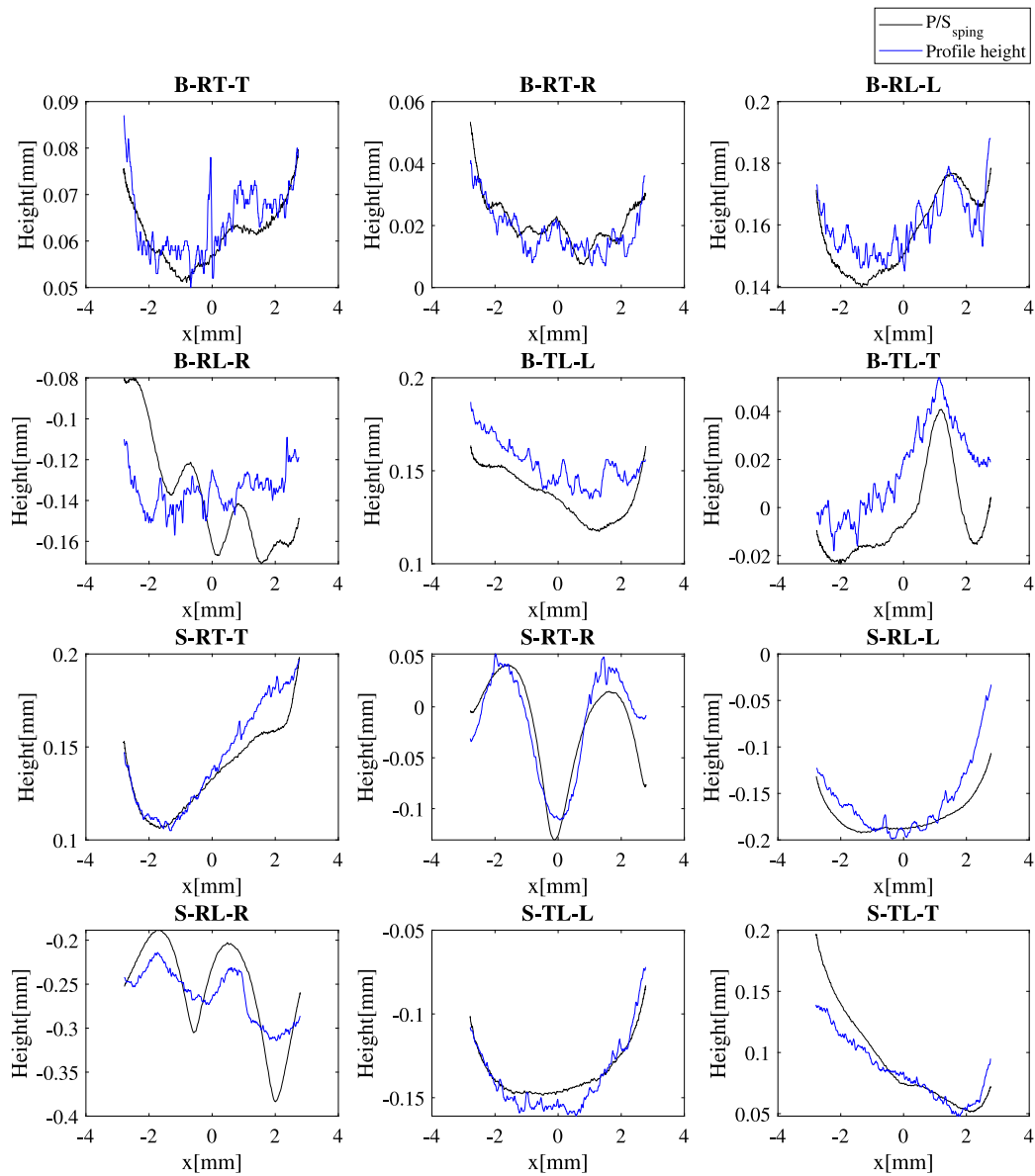
Acknowledgments

Fig. A.2. Comparison of line profile height (measured after the tests) and relative normal displacement for all test cases.

Appendix

The surface profile of all test cases (measured at the end of the tests) are shown in Fig. A.1, and the profile height of the white lines is then compared with the deformation of the spring in Fig. A.2. Results show that for most cases the variation of the spring deformation fits that of the line profile except for test case B-RL-R and S-RL-R. In those two cases, the variation of the spring deformation is larger than that of the line profile. For these cases, we hypothesize that there are other factors also influencing the normal force variation. For example, one factor could be that the differences between the elastic modulus of earlywood and latewood is much larger in these two cases, which leads to larger variation of the normal displacement of the steel sphere. This may cause additional hysteresis terms due to surface deformation, as indicated by the friction theory of Bowden and Tabor [18]. The other factor could be due to the presence of the ploughing effect during the sliding phase. The absence of the hysteresis term and the ploughing terms in the optimization procedure could cause much larger error in using Eqs. (4)–(5) to get the approximate slope of the trajectory of the steel sphere k, therefore, the minimum cost function value for those

two cases are larger than other test cases on the same wood sample as shown in Fig. 14.

References

[1] Hegeir OA, Kvande T, Stamatopoulos H, Bohne RA. Comparative life cycle analysis of timber, steel and reinforced concrete portal frames: A theoretical study on a Norwegian industrial building. Buildings 2022;12(5).
[2] Duan Z, Huang Q, Zhang Q. Life cycle assessment of mass timber construction: A review. Build Environ 2022;221:109320.
[3] Giulia A, Fabrizio M, Milena M, Spartaco P. Performance assessment of timber high-rise buildings: Structural and technological considerations. Open Constr Build Technol J 2022;16(1).
[4] Ilgın HE, Karjalainen M, Pelsmakers S. Contemporary tall residential timber buildings: what are the main architectural and structural design considerations? Int J Build Pathol Adapt 2023;41(6):26–46.
[5] Van De Kuilen J, Ceccotti A, Xia Z, He M. Very tall wooden buildings with cross laminated timber. Procedia Eng 2011;14:1621–8.
[6] Friedrich K, Akpan E, Wetzel B. On the tribological properties of extremely different wood materials. Eur J Wood Wood Prod 2021;79(4):977–88.
[7] Wu Z, Guo Z, Yuan C. Insight into the influence of the anatomical properties of wood on the tribological properties. J Clean Prod 2022;330:129800.
[8] Dong C, Yang Y, Yuan C, Bai X, Guo Z. Effects of anisotropy of lignum vitae wood on its tribological performances. Composites B 2022;228:109426.

[9] Wu Y, Xie Q, Lin H, Zhang L, Yang H. Seismic behavior of variable friction timber dampers: Experimental and numerical investigation. J Build Eng 2022;53:104591.

[10] Mourya V, Bhore SP. Experimental investigation and optimization of tribological characteristics of wooden journal bearings. Biotribology 2023;35:100241.

[11] Mirra M, Ravenshorst G, de Vries P, Messali F. Experimental characterisation of as-built and retrofitted timber-masonry connections under monotonic, cyclic and dynamic loading. Constr Build Mater 2022;358:129446.

[12] Rautkari L, Kutnar A, Hughes M, Kamke FA. Mass-timber structures—Increased ductility through friction mechanism. In: Proceedings of the architectural engineering conference 2019. 2019, p. 316–26.

[13] Fitzgerald D, Miller TH, Sinha A, Nairn JA. Cross-laminated timber rocking walls with slip-friction connections. Eng Struct 2020;220:110973.

[14] Wakashima Y, Ishikawa K, Shimizu H, Kitamori A, Matsubara D, Tesfamariam S. Dynamic and long-term performance of wood friction connectors for timber shear walls. Eng Struct 2021;241:112351.

[15] De Santis Y, Sciomenta M, Spera L, Rinaldi V, Fragiacomo M, Bedon C. Effect of interlayer and inclined screw arrangements on the load-bearing capacity of timber-concrete composite connections. Buildings 2022;12(12).

[16] He M, Zhang Q, Sun X, Alhaddad W. An experimental and numerical study on the shear performance of friction-type high-strength bolted connections used for CLT-steel hybrid shear walls. Eng Struct 2024;306:117868.

[17] Wakashima Y, Ishikawa K, Shimizu H, Kitamori A, Matsubara D, Hanai S, et al. Friction-based connectors with wooden dowels for timber shear walls: Shake table and time-dependent test. Eng Struct 2024;307:117838.

[18] Atack D, Tabor D. The friction of wood. Proc R Soc Lond Ser A Math Phys Eng Sci 1958;246(1247):539–55.

[19] McLaren K, Tabor D. The frictional properties of lignum vitae. Br J Appl Phys 1961;12(3):118.

[20] McKenzie W, Karpovich H. The frictional behaviour of wood. Wood Sci Technol 1968;2(2):139–52.

[21] Lemoine TJ, McMillin CW, Manwiller F. Wood variables affecting the friction coefficient of spruce pine on steel. Wood Sci 1970;2(3):144–8.

[22] Guan N, Thunell B, Lyth K. On the friction between steel and some common Swedish wood species. Holz als Roh- und Werkstoff 1983;41(2):55–60.

[23] Vaz MF, Fortes M. Friction properties of cork. J Mater Sci 1998;33:2087–93.

[24] Svensson B, Rundlöf M, Höglund H. Sliding friction between wood and steel in a saturated steam environment. J Pulp Pap Sci 2006;32(1):38–43.

[25] Svensson BA, Nyström S, Gradin PA, Höglund H. Frictional testing of wood—Initial studies with a new device. Tribol Int 2009;42(1):190–6.

[26] Mulvihill DM, Kartal ME, Olver A, Nowell D, Hills D. Investigation of non-Coulomb friction behaviour in reciprocating sliding. Wear 2011;271(5–6):802–16.

[27] Fantetti A, Tamatam LR, Volvert M, Lawal I, Liu L, Salles L, et al. The impact of fretting wear on structural dynamics: Experiment and simulation. Tribol Int 2019;138:111–24.

[28] Li D, Botto D, Xu C, Gola M. Fretting wear of bolted joint interfaces. Wear 2020;458:203411.

[29] Jin X, Sun W, Shipway P. Derivation of a wear scar geometry-independent coefficient of friction from fretting loops exhibiting non-Coulomb frictional behaviour. Tribol Int 2016;102:561–8.

[30] Hintikka J, Lehtovaara A, Mäntylä A. Normal displacements in non-Coulomb friction conditions during fretting. Tribol Int 2016;94:633–9.

[31] Llavori I, Zabala A, Aginagalde A, Tato W, Ayerdi J, Gómez X. Critical analysis of coefficient of friction derivation methods for fretting under gross slip regime. Tribol Int 2020;143:105988.

[32] De Wit CC, Olsson H, Astrom KJ, Lischinsky P. A new model for control of systems with friction. IEEE Trans Autom Control 1995;40(3):419–25.

[33] Forest Products Laboratory (US). Wood handbook: wood as an engineering material, (72). Forest Products Laboratory(FPL); 1987.

[34] Blau PJ. Friction science and tecnology: From concepts to applications. second ed. Boca Raton, USA: CRC Press, Taylor and Francis; 2009.

[35] Hirata S, Ohta M, Honma Y. Hardness distribution on wood surface. J Wood Sci 2001;47:1–7.

[36] Yin W, Liu Z, Tian P, Tao D, Meng Y, Han Z, et al. Tribological properties of wood as a cellular fiber-reinforced composite. Biotribology 2016;5:67–73.

[37] Fouvry S, Duó P, Perruchaut P. A quantitative approach of Ti–6Al–4V fretting damage: friction, wear and crack nucleation. Wear 2004;257(9–10):916–29.

[38] Ismail M, Ikhouane F, Rodellar J. The hysteresis Bouc-Wen model, a survey. Arch Comput Methods Eng 2009;16:161–88.

[39] Cabboi A, Woodhouse J. Validation of a constitutive law for friction-induced vibration under different wear conditions. Wear 2018;396–397:107–25.

[40] Cabboi A, Marino L, Cicirello A. A comparative study between Amontons–Coulomb and Dieterich–Ruina friction laws for the cyclic response of a single degree of freedom system. Eur J Mech A Solids 2022;96:104737.